

Deterministic ion-photon qubit exchange in realistic ion cavity-QED systems without strong coupling

Adrien Borne^{1,2} and Barak Dayan^{1,*}

¹*AMOS and Department of Chemical and Biological Physics,
Weizmann Institute of Science, Rehovot 76100, Israel*

²*Laboratoire Matériaux et Phénomènes Quantiques,
Université Paris Diderot, CNRS, UMR 7162, 75013 Paris, France*

(Dated: June 19, 2022)

Deterministic ion-photon qubit exchange - a highly desirable building block for quantum information networks - is typically assumed to require strong coupling, namely having the single-photon Rabi frequency be the fastest rate in the system. Yet this assumption is incorrect. Specifically, the two native photon-atom gates demonstrated to date (C-phase and SWAP) require only Purcell enhancement that corresponds to moderate single-atom cooperativities. This implies that small mode volume cavities - which are extremely challenging to incorporate with ions due to the difficulty of trapping them close to dielectric surfaces - are unnecessary. Instead, larger cavities that are more compatible with the trap apparatus are enough, as long as their numerical aperture is high enough to maintain a small mode area at the ion's position. Here we outline the details of a scheme for a deterministic ion-photon SWAP gate based on realistic cavity-QED systems with $^{171}\text{Yb}^+$, $^{40}\text{Ca}^+$ and $^{138}\text{Ba}^+$ ions. We define the optimal coupling and detuning parameters and simulate the resulting fidelities and efficiencies of the gate, demonstrating that highly efficient photon-ion two-qubit gates indeed do not require strong coupling and are practically attainable with current experimental capabilities.

I. INTRODUCTION

Efficient ion-photon qubit exchange is a vital building-block for the modular scaling-up of ion-based quantum information systems [1–5]. Most current experimental efforts to realize such an ion-photon interface [6–20] aim at obtaining the highest possible atom-cavity coupling rate (g , also termed single-photon Rabi frequency) in order to reach the strong-coupling regime, i.e. the regime in which g is the fastest rate in the system [21]. Since g is inversely proportional to the square root of the cavity mode volume: $g \propto 1/\sqrt{V}$, this implies tiny cavities (< 1 mm), which in turn make the stability of the trap very challenging due to the proximity of the ion to dielectric surfaces [22, 23].

In contrast, the two native atom-photon gates demonstrated to date, the controlled-phase gate (suggested by Duan and Kimble [24] and demonstrated experimentally in [25]) and SWAP (suggested in [26], theoretically studied in [27–32] and demonstrated in [33]) do not strictly require strong coupling. Both gates do require high cooperativity $C = g^2/\kappa\gamma \gg 1$, where κ is the cavity decay rate and γ the spontaneous emission rate of the atom into free space. This essentially corresponds to Purcell enhancement and is proportional to Q/V , with Q being the quality factor of the cavity [34]. While this may suggest that small mode volume is required, note that both Q and V scale linearly with the cavity round-trip length: this means that the Purcell enhancement - and the cooperativity - are in fact proportional to F/A , with A being

the mode area and F the finesse of the cavity, namely the cavity lifetime in units of the round-trip time. Although this distinction may seem trivial, in ionic systems this is crucial as it allows placing ions far away from dielectrics.

In this work we wish to demonstrate quantitatively the feasibility and potential of realizing photon-ion qubits gates in practical systems. We do so by analyzing in detail the implementation of a photon-ion SWAP gate similar to that demonstrated with neutral atoms [33]. The underlying mechanism, namely the single-photon Raman interaction (SPRINT), and the system are described in the following Sec. II. We then perform an analytical description in Sec. III, which allows us to quantify the performance of the swap process by calculating its fidelity and efficiency for arbitrary ionic and photonic qubits. In Sec. IV, we finally apply our results to realistic situations with ions of $^{171}\text{Yb}^+$, $^{40}\text{Ca}^+$ and $^{138}\text{Ba}^+$, analytically when the system is invariant under qubit rotation, and numerically otherwise. We indeed see that high cooperativity is required, but not strong coupling. Also, we show that a proper choice of cavity coupling and detuning rates (cavity-field, cavity-ion and potentially Zeeman detunings) leads to an optimization of the gate performance.

II. REALIZATION OF AN ION-PHOTON SWAP GATE

A. The underlying mechanism: single-photon Raman interaction

The implementation of the ion-photon SWAP gate under study in this paper relies on a scheme called single-

* barak.dayan@weizmann.ac.il

photon Raman interaction (SPRINT) [26–32]. Owing to quantum interference, it allows a single photon to deterministically control the state of a single quantum emitter, and vice versa. SPRINT requires a three-level Λ -system to couple independently each of two optical modes (\hat{a} and \hat{b}) forming a photonic qubit to one of the two ground states ($|\downarrow\rangle$ and $|\uparrow\rangle$) forming a material qubit; that is, the optical mode \hat{a} (resp. \hat{b}) drives the transition $|\downarrow\rangle - |e\rangle$ (resp. $|\uparrow\rangle - |e\rangle$). As depicted in Fig. 1(a) and provided that the two transitions are of equal strength, an incoming probe field of one photon in the mode \hat{a} interacting with the quantum emitter in the state $|\downarrow\rangle$ destructively interferes with the field radiated in the same mode \hat{a} , phase-shifted by π . This leads the system to emit a photon in the mode \hat{b} , forcing a Raman transfer of the quantum emitter from $|\downarrow\rangle$ to $|\uparrow\rangle$ [26–32]. On the other hand, a probe in the mode \hat{a} does not interact with the quantum emitter in $|\uparrow\rangle$, leaving the entire system unchanged as depicted in Fig. 1(b). This nonlinear interaction at the

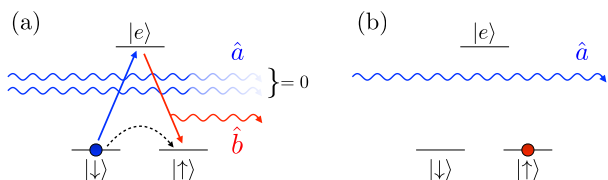


Figure 1. Operating principle of single-photon Raman interaction. (a) Destructive interference between the optical fields in the mode \hat{a} forces the emission of the photon in the mode \hat{b} together with the toggle of the quantum emitter from the state $|\downarrow\rangle$ to $|\uparrow\rangle$. (b) Both the states of the photon ($|1_a\rangle$) and quantum emitter ($|\uparrow\rangle$) are unchanged.

level of a photon is also a coherent process, hence more generally applies both to the photonic and the material qubits defined above where it acts as a SWAP gate between them. Under SPRINT, the photon-emitter joint state is indeed modified as follows:

$$(c_a |1_a\rangle + c_b |1_b\rangle)_{\text{photon}} \otimes (c_\downarrow |\downarrow\rangle + c_\uparrow |\uparrow\rangle)_{\text{emitter}} \rightarrow (c_\uparrow |1_a\rangle - c_\downarrow |1_b\rangle)_{\text{photon}} \otimes (-c_b |\downarrow\rangle + c_a |\uparrow\rangle)_{\text{emitter}}. \quad (1)$$

B. Implementation with a single ion trapped in a Fabry-Perot cavity

This ion-photon SWAP gate can then be implemented by coupling an ion, in which we identify a three-level Λ -system, to the optical modes through a Fabry-Perot resonator, which provides the necessary interaction enhancement. It has been shown in [32] that this process can reach unit fidelity by properly choosing the cavity coupling rate so as to reach complete destructive interference between the probe and the field radiated in the same mode, provided that the two following

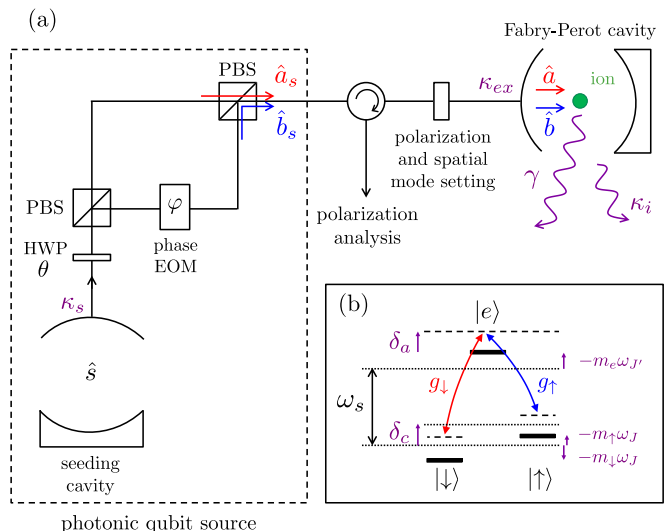


Figure 2. Schematic of the theoretical model. (a) The optical setup consisting of a seeding single-sided cavity to generate the photonic qubits and an ion trapped in a second single-sided cavity. (b) The relevant three-level Λ -system describing the ion. HWP stands for half-wave plate, PBS for polarizing beam splitter and EOM for electro-optic modulator. The various rates and spectral detunings are explicated in the main text.

conditions are met: (i) the intrinsic loss rate of the resonator must be smaller than the cavity field decay rate, and (ii) the spontaneous emission must be mostly directed into the cavity modes, i.e. $C \gg 1$ as stated in the introduction. Note that the coupling rate to the Fabry-Perot resonator is set by the input-output mirror transmission and therefore cannot be fine-tuned, which can reduce the fidelity of the operation. This differs from the case of nanofiber-coupled whispering-gallery mode microresonators (as performed in demonstrations with neutral atoms [33, 35, 36]), in which coupling rates can continuously be tuned to reach a value optimizing the fidelity. Still, in the case of Fabry-Perot microresonators, we will show in the following that it is possible to circumvent this issue and restore the fidelity by properly setting frequency detuning parameters, at the cost of a reduced efficiency.

We describe SPRINT in the framework of cascaded systems [30, 32, 37] as shown in Fig. 2. A single-photon input pulse of frequency ω_s and linearly polarized is modeled by introducing a single-sided seeding cavity described by its annihilation operator \hat{s} , which emits with a decay rate $2\kappa_s$. A half-wave plate (with angle $\theta/4$ between its fast axis and the incident polarization) and a Mach-Zehnder interferometer composed of two polarizing beam splitters (PBS) with an electro-optic phase modulator (phase φ) in one arm enable to define two orthogonal seeding modes of polarization \hat{a}_s and \hat{b}_s such that $\hat{s} = \cos(\theta/2)\hat{a}_s + \sin(\theta/2)e^{i\varphi}\hat{b}_s$. The photon then couples

to two orthogonal polarization modes \hat{a} and \hat{b} of a single-sided Fabry-Perot resonator at a rate $2\kappa_{ex}$. Although the second mirror of the single-sided cavity is ideally a perfect reflector, we account for its experimental non-zero transmission as well as for absorption and scattering, as the intrinsic cavity loss occurring at a rate $2\kappa_i$. The total cavity loss is denoted $2\kappa_t = 2(\kappa_{ex} + \kappa_i)$.

The ion trapped in the resonator can then interact with the photon through the transition from the ground state $|\downarrow\rangle$ (resp. $|\uparrow\rangle$) to the excited state $|e\rangle$, described by the lowering operators $\hat{\sigma}_{\downarrow e} = |\downarrow\rangle\langle e|$ (resp. $\hat{\sigma}_{\uparrow e} = |\uparrow\rangle\langle e|$), at the rates $2g_{\downarrow}$ (resp. $2g_{\uparrow}$). We denote \mathcal{C}_{\downarrow} and \mathcal{C}_{\uparrow} the Clebsch-Gordan coefficients associated with these two transitions, and g such that $g_{\downarrow,\uparrow} = \mathcal{C}_{\downarrow,\uparrow}g$. The ion can also spontaneously emit in free space at the rate denoted 2γ . Finally, the polarization of the field exiting the cavity is analyzed.

Since SPRINT relies on destructive interference between the incoming probe and the field radiated by the quantum emitter in the same mode as the probe, a non-perfect spatial overlap of these beams will damage the fidelity of the interaction. For instance, a spatial mode matching of 90% ([38]) leads to about 5% reduction in fidelity, assuming centered Gaussian beams. It is nonetheless possible to preserve it by shaping the transverse mode of the probe before the cavity.

In the following development, the system is modeled by considering the general case of an asymmetric Λ -system, i.e. not invariant under rotation of the Bloch sphere, which can be due to different Clebsch-Gordan coefficients or degeneracy lifting of the Zeeman sublevels. It is therefore here necessary to consider in our description arbitrary input superposition states, unlike in Ref. [32] where the symmetry of the Λ -system allowed to consider both photonic and atomic states as poles of the Bloch sphere.

III. THEORETICAL MODEL

The dynamics of the system is given by the following Hamiltonian in a frame rotating at the probe frequency ω_s ($\hbar = 1$):

$$\hat{H} = \hat{H}_{\text{drive}} + \hat{H}_{\text{field}} + \hat{H}_{\text{atom}} + \hat{H}_{\text{int}}, \quad (2a)$$

$$\hat{H}_{\text{drive}} = -2i\sqrt{\kappa_s\kappa_{ex}}(\hat{a}_s\hat{a}^\dagger + \hat{b}_s\hat{b}^\dagger) - i\kappa_s\hat{s}^\dagger\hat{s}, \quad (2b)$$

$$\begin{aligned} \hat{H}_{\text{field}} = & -i[\kappa_t + i(\delta_c - m_{\downarrow}\omega_J)]\hat{a}^\dagger\hat{a} \\ & -i[\kappa_t + i(\delta_c - m_{\uparrow}\omega_J)]\hat{b}^\dagger\hat{b}, \end{aligned} \quad (2c)$$

$$\hat{H}_{\text{ion}} = -i[\gamma + i(\delta_a - m_e\omega_{J'})]\hat{\sigma}_{ee}, \quad (2d)$$

$$\hat{H}_{\text{int}} = (g_{\downarrow}^*\hat{a}^\dagger\hat{\sigma}_{\downarrow e} + g_{\downarrow}\hat{\sigma}_{\downarrow e}^\dagger\hat{a}) + (g_{\uparrow}\hat{b}^\dagger\hat{\sigma}_{\uparrow e} + g_{\uparrow}^*\hat{\sigma}_{\uparrow e}^\dagger\hat{b}), \quad (2e)$$

where $\hat{\sigma}_{ee} = |e\rangle\langle e|$ is the population of the excited state. The probe frequency is detuned from the cavity resonance by δ_c , and from the atomic transition by δ_a . An

applied magnetic field \vec{B} lifts the degeneracy in the total angular momentum and shifts the energy of each of the Zeeman sublevels of magnetic quantum numbers m_{\downarrow} , m_{\uparrow} and m_e . The Larmor frequencies associated with the levels $^{2S+1}L_{J,J'}$ are $\omega_{J,J'} = \mu_B g_{J,J'} B$ with μ_B the Bohr magneton and $g_{J,J'}$ the Landé factors. The non-Hermitian term \hat{H}_{drive} accounts for the unidirectional interaction between the seeding cavity and the system. \hat{H}_{field} and \hat{H}_{ion} are the optical field and ion Hamiltonians, which include losses and detunings, and \hat{H}_{int} is the Jaynes-Cummings term describing the photon-ion interaction.

In the Hilbert space $\mathcal{H} = \mathcal{H}_s \otimes \mathcal{H}_a \otimes \mathcal{H}_b \otimes \mathcal{H}_{\text{ion}}$, where \mathcal{H}_s is associated to the seeding cavity, \mathcal{H}_a and \mathcal{H}_b to the optical modes \hat{a} and \hat{b} , and \mathcal{H}_{ion} to the state of the atom, the initial state can be written:

$$|\psi(0)\rangle = (\alpha|1_{a,s}\rangle + \beta|1_{b,s}\rangle) \otimes |0_a, 0_b\rangle \otimes (\alpha'|\downarrow\rangle + \beta'|\uparrow\rangle), \quad (3)$$

where $|\alpha|^2 + |\beta|^2 = |\alpha'|^2 + |\beta'|^2 = 1$, $\alpha = \cos(\theta/2)$ and $\beta = \sin(\theta/2)e^{i\varphi}$.

According to the Schrödinger equation, the state evolves as

$$\begin{aligned} |\psi(t)\rangle = & e^{-\kappa_s t} [\alpha\alpha'|1_{a,s}, 0_a, 0_b, \downarrow\rangle + \alpha\beta'|1_{a,s}, 0_a, 0_b, \uparrow\rangle \\ & + \beta\alpha'|1_{b,s}, 0_a, 0_b, \downarrow\rangle + \beta\beta'|1_{a,s}, 0_a, 0_b, \uparrow\rangle] \\ & + c_1(t)|0_s, 1_a, 0_b, \downarrow\rangle + c_2(t)|0_s, 1_a, 0_b, \uparrow\rangle \quad (4) \\ & + c_3(t)|0_s, 0_a, 1_b, \downarrow\rangle + c_4(t)|0_s, 0_a, 1_b, \uparrow\rangle \\ & + c_5(t)|0_s, 0_a, 0_b, e\rangle, \end{aligned}$$

where

$$\begin{aligned} \dot{c}_1(t) = & -2\alpha\alpha'\sqrt{\kappa_s\kappa_{ex}}e^{-\kappa_s t} \\ & - (\kappa_t + i\delta_{\downarrow})c_1(t) - ig_{\downarrow}^*c_5(t), \end{aligned} \quad (5a)$$

$$\dot{c}_2(t) = -2\alpha\beta'\sqrt{\kappa_s\kappa_{ex}}e^{-\kappa_s t} - (\kappa_t + i\delta_{\downarrow})c_2(t), \quad (5b)$$

$$\dot{c}_3(t) = -2\beta\alpha'\sqrt{\kappa_s\kappa_{ex}}e^{-\kappa_s t} - (\kappa_t + i\delta_{\uparrow})c_3(t), \quad (5c)$$

$$\begin{aligned} \dot{c}_4(t) = & -2\beta\beta'\sqrt{\kappa_s\kappa_{ex}}e^{-\kappa_s t} \\ & - (\kappa_t + i\delta_{\uparrow})c_4(t) - ig_{\uparrow}c_5(t), \end{aligned} \quad (5d)$$

$$\dot{c}_5(t) = -ig_{\downarrow}c_1(t) - ig_{\uparrow}^*c_4(t) - (\gamma + i\delta_e)c_5(t), \quad (5e)$$

and introducing the following notations

$$\delta_{\downarrow} := \delta_c - m_{\downarrow}\omega_J, \quad (6a)$$

$$\delta_{\uparrow} := \delta_c - m_{\uparrow}\omega_J, \quad (6b)$$

$$\delta_e := \delta_a - m_e\omega_{J'}. \quad (6c)$$

Provided that the driving pulse is long enough such that κ_s is the lowest rate of the system, Eq. 5 are solved by taking $d|\psi(t)\rangle/dt = 0$ at all times. This steady-state solution gives:

$$c_1(t) = 2 \frac{\sqrt{\kappa_s \kappa_{ex}}}{\kappa_t + i\delta_\downarrow} e^{-\kappa_s t} \times \left[\frac{2\tilde{C}_t}{1 + 2\tilde{C}_t} \frac{\alpha\alpha' |g_\downarrow|^2 (\kappa_t + i\delta_\uparrow) + \beta\beta' g_\downarrow^* g_\uparrow^* (\kappa_t + i\delta_\downarrow)}{|g_\downarrow|^2 (\kappa_t + i\delta_\uparrow) + |g_\uparrow|^2 (\kappa_t + i\delta_\downarrow)} - \alpha\alpha' \right], \quad (7a)$$

$$c_2(t) = -2\alpha\beta' \frac{\sqrt{\kappa_s \kappa_{ex}}}{\kappa_t + i\delta_\downarrow} e^{-\kappa_s t}, \quad (7b)$$

$$c_3(t) = -2\alpha'\beta \frac{\sqrt{\kappa_s \kappa_{ex}}}{\kappa_t + i\delta_\uparrow} e^{-\kappa_s t}, \quad (7c)$$

$$c_4(t) = 2 \frac{\sqrt{\kappa_s \kappa_{ex}}}{\kappa_t + i\delta_\uparrow} e^{-\kappa_s t} \times \left[\frac{2\tilde{C}_t}{1 + 2\tilde{C}_t} \frac{\alpha\alpha' g_\downarrow g_\uparrow (\kappa_t + i\delta_\uparrow) + \beta\beta' |g_\uparrow|^2 (\kappa_t + i\delta_\downarrow)}{|g_\downarrow|^2 (\kappa_t + i\delta_\uparrow) + |g_\uparrow|^2 (\kappa_t + i\delta_\downarrow)} - \beta\beta' \right], \quad (7d)$$

$$c_5(t) = 2i\sqrt{\kappa_s \kappa_{ex}} e^{-\kappa_s t} \frac{2\tilde{C}_t}{1 + 2\tilde{C}_t} \times \frac{\alpha\alpha' g_\downarrow (\kappa_t + i\delta_\uparrow) + \beta\beta' g_\uparrow^* (\kappa_t + i\delta_\downarrow)}{|g_\downarrow|^2 (\kappa_t + i\delta_\uparrow) + |g_\uparrow|^2 (\kappa_t + i\delta_\downarrow)}, \quad (7e)$$

with \tilde{C}_t a complex quantity defined as follows:

$$\tilde{C}_t = \frac{1}{2(\gamma + i\delta_e)} \left(\frac{|g_\downarrow|^2}{\kappa_t + i\delta_\downarrow} + \frac{|g_\uparrow|^2}{\kappa_t + i\delta_\uparrow} \right). \quad (8)$$

Note that when $\delta_\uparrow = \delta_\downarrow = \delta_e = 0$, \tilde{C}_t is the total cooperativity C_t and quantifies the preferential spontaneous emission of the ion in the cavity modes rather than in free space.

Using the input-output formalism [39], two cavity output modes \hat{a}_{out} and \hat{b}_{out} are defined as follows:

$$\hat{a}_{out} = \sqrt{2\kappa_s} \hat{a}_s + \sqrt{2\kappa_{ex}} \hat{a}, \quad (9a)$$

$$\hat{b}_{out} = \sqrt{2\kappa_s} \hat{b}_s + \sqrt{2\kappa_{ex}} \hat{b}. \quad (9b)$$

These operators can be conveniently rewritten in a basis

that describes the bright and dark states of the outgoing photon by using the following beam splitter equations:

$$\hat{D}_{out} = \alpha' \hat{a}_{out} + \beta' \hat{b}_{out}, \quad (10a)$$

$$\hat{B}_{out} = \beta' \hat{a}_{out} - \alpha' \hat{b}_{out}, \quad (10b)$$

where α' and β' , defining the atomic qubit, are also the reflection and transmission coefficients of the beam splitter respectively. It is indeed expected that the outgoing photon carry the initial state of the atom and will exit through the bright port of that fictitious beam splitter. In the case of an atomic qubit defined as a pole state of the Bloch sphere, the dark and bright modes simply reduce to the modes \hat{a} and \hat{b} .

The probabilities for a single photon to exit the cavity in the dark and bright states are then given by:

$$\begin{aligned} P_D &= \int_0^\infty \langle \hat{D}_{out}^\dagger \hat{D}_{out} \rangle dt \\ &= \left| \alpha' (\alpha\alpha' + \beta\beta') + \sqrt{\frac{\kappa_{ex}}{\kappa_s}} (\alpha' c_1(0) + \beta' c_3(0)) \right|^2 + \left| \alpha' (\alpha\alpha' + \beta\beta') + \sqrt{\frac{\kappa_{ex}}{\kappa_s}} (\alpha' c_2(0) + \beta' c_4(0)) \right|^2 \\ &= \alpha'^2 \left| \alpha\alpha' \left(1 - \frac{2\kappa_{ex}}{\kappa_t + i\delta_\downarrow} \right) + \beta\beta' \left(1 - \frac{2\kappa_{ex}}{\kappa_t + i\delta_\uparrow} \right) + \frac{2\kappa_{ex}}{\kappa_t + i\delta_\downarrow} \frac{2\tilde{C}_t}{1 + 2\tilde{C}_t} \frac{\alpha\alpha' |g_\downarrow|^2 (\kappa_t + i\delta_\uparrow) + \beta\beta' g_\downarrow^* g_\uparrow^* (\kappa_t + i\delta_\downarrow)}{|g_\downarrow|^2 (\kappa_t + i\delta_\uparrow) + |g_\uparrow|^2 (\kappa_t + i\delta_\downarrow)} \right|^2 \\ &\quad + \beta'^2 \left| \alpha\alpha' \left(1 - \frac{2\kappa_{ex}}{\kappa_t + i\delta_\downarrow} \right) + \beta\beta' \left(1 - \frac{2\kappa_{ex}}{\kappa_t + i\delta_\uparrow} \right) + \frac{2\kappa_{ex}}{\kappa_t + i\delta_\uparrow} \frac{2\tilde{C}_t}{1 + 2\tilde{C}_t} \frac{\alpha\alpha' g_\downarrow g_\uparrow (\kappa_t + i\delta_\uparrow) + \beta\beta' |g_\uparrow|^2 (\kappa_t + i\delta_\downarrow)}{|g_\downarrow|^2 (\kappa_t + i\delta_\uparrow) + |g_\uparrow|^2 (\kappa_t + i\delta_\downarrow)} \right|^2, \end{aligned} \quad (11)$$

$$\begin{aligned} P_B &= \int_0^\infty \langle \hat{B}_{out}^\dagger \hat{B}_{out} \rangle dt \\ &= \left| \alpha' (\alpha\beta' - \beta\alpha') + \sqrt{\frac{\kappa_{ex}}{\kappa_s}} (\beta' c_1(0) - \alpha' c_3(0)) \right|^2 + \left| \beta' (\alpha\beta' - \beta\alpha') + \sqrt{\frac{\kappa_{ex}}{\kappa_s}} (\beta' c_2(0) - \alpha' c_4(0)) \right|^2 \end{aligned} \quad (12)$$

$$\begin{aligned}
&= \left| \alpha\alpha'\beta' \left(1 - \frac{2\kappa_{ex}}{\kappa_t + i\delta_\downarrow} \right) - \beta\alpha'^2 \left(1 - \frac{2\kappa_{ex}}{\kappa_t + i\delta_\uparrow} \right) + \beta' \frac{2\kappa_{ex}}{\kappa_t + i\delta_\downarrow} \frac{2\tilde{C}_t}{1 + 2\tilde{C}_t} \frac{\alpha\alpha'|g_\downarrow|^2(\kappa_t + i\delta_\uparrow) + \beta\beta'g_\downarrow^*g_\uparrow^*(\kappa_t + i\delta_\downarrow)}{|g_\downarrow|^2(\kappa_t + i\delta_\uparrow) + |g_\uparrow|^2(\kappa_t + i\delta_\downarrow)} \right|^2 \\
&+ \left| \alpha\beta'^2 \left(1 - \frac{2\kappa_{ex}}{\kappa_t + i\delta_\downarrow} \right) - \beta\alpha'\beta' \left(1 - \frac{2\kappa_{ex}}{\kappa_t + i\delta_\uparrow} \right) - \alpha' \frac{2\kappa_{ex}}{\kappa_t + i\delta_\uparrow} \frac{2\tilde{C}_t}{1 + 2\tilde{C}_t} \frac{\alpha\alpha'g_\downarrow g_\uparrow(\kappa_t + i\delta_\uparrow) + \beta\beta'|g_\uparrow|^2(\kappa_t + i\delta_\downarrow)}{|g_\downarrow|^2(\kappa_t + i\delta_\uparrow) + |g_\uparrow|^2(\kappa_t + i\delta_\downarrow)} \right|^2.
\end{aligned}$$

Note that these expressions reduce to that of Ref. [32] when the detunings are set to zero and for pole states of the Bloch sphere, e.g. $\alpha = \alpha' = 1$.

We now quantify the operation of the SWAP gate by defining its fidelity \mathcal{F} , a figure of merit defined as the overlap of the final state with the expected state. For a given initial state defined by the set of parameters $\{\alpha, \alpha'\} \in [0, 1]^2$,

$$\mathcal{F}(\alpha, \alpha') = \frac{P_B}{P_B + P_D} \quad (13)$$

and $\eta(\alpha, \alpha') = P_B + P_D$ is the efficiency of the process. We denote $\bar{\mathcal{F}}$ and $\bar{\eta}$ the average fidelity and efficiency over the initial states.

P_D originates from non-perfect destructive interference between the probe and the field radiated in the same mode as the probe because of intrinsic losses and limited cooperativity. Hence, in order to achieve unit swap fidelity, both the real and the imaginary parts of P_D can be set to zero in Eq. 11. We obtain

$$g_\uparrow = g_\downarrow^*, \quad (14a)$$

$$\omega_J = \omega_{J'} = 0 \Rightarrow \delta_\downarrow = \delta_\uparrow = \delta_c \text{ and } \delta_e = \delta_a. \quad (14b)$$

Unit fidelity can then only be reached in symmetric Λ -systems, whose degenerated transitions have equal Clebsch-Gordan coefficients.

κ_{ex} is set by the transmission of the coupling mirror and is therefore not a good tuning parameter unlike in Ref. [32]. However, unit fidelity is found by setting both the probe-cavity and atom-cavity detunings to the following optimal values:

$$\delta_c^{\text{opt}} = \pm \left[\kappa_i \sqrt{4\kappa_{ex}^2(1 + C_i) + \kappa_i^2 C_i^2} - \kappa_{ex}^2 - (1 + C_i)\kappa_i^2 \right]^{1/2}, \quad (15a)$$

$$\delta_a^{\text{opt}} = \frac{\kappa_i \gamma}{2\delta_c^{\text{opt}}} \left(2 + 3C_i - \sqrt{4\frac{\kappa_{ex}^2}{\kappa_i^2}(1 + C_i) + C_i^2} \right), \quad (15b)$$

with $C_i = \frac{|g_{\downarrow, \uparrow}|^2}{\kappa_i \gamma}$ the intrinsic cooperativity.

δ_c^{opt} and δ_a^{opt} being real parameters, Eqs. 15 only have valid solutions for $\kappa_i \leq \kappa_i \sqrt{1 + 2C_i} := \kappa_{ex}^{\text{opt}}$, where κ_{ex}^{opt} is the optimal coupling to the cavity [32]. Specifically, when $\kappa_{ex} = \kappa_{ex}^{\text{opt}}$, the system already gives an unit fidelity and no detuning is needed; when $\kappa_{ex} < \kappa_{ex}^{\text{opt}}$, unit

fidelity can be retrieved by tuning the previous detunings according to Eq. 15, at the expense of a decrease of the efficiency; and when $\kappa_{ex} > \kappa_{ex}^{\text{opt}}$, no correction can be here performed using these detuning parameters. It is therefore best to design the experiment by choosing a coupling mirror transmission such that $\kappa_{ex} \lesssim \kappa_{ex}^{\text{opt}}$, the fine-tuning optimization being performed by setting δ_c^{opt} and δ_a^{opt} .

Regarding the efficiency of the process, it is affected by the intrinsic losses and the spontaneous emission of the ion to free space. Whether the previous optimization of the fidelity is performed or not, the following upper bound holds:

$$\eta \leq \eta_{\text{max}} = \left(\frac{C_i}{\sqrt{1 + 2C_i} + (1 + C_i)} \right)^2. \quad (16)$$

We turn next to the case where $g_\uparrow \neq g_\downarrow$. Although the fidelity will not reach one, its optimization can still be performed numerically by setting $\partial_d F = 0$ with $d \in \{\delta_\downarrow, \delta_\uparrow, \delta_e\}$, i.e. $P_D \cdot \partial_d P_B = P_B \cdot \partial_d P_D$ averaged over all $\{\alpha, \alpha'\} \in [0, 1]^2$ as the system is no longer symmetric under qubit rotations. This procedure then leads to a set of optimal parameters $\{\delta_c^{\text{opt}}, \delta_a^{\text{opt}}, B^{\text{opt}}\}$. Note that it may indeed be helpful in this situation to lift the degeneracy of the Zeeman sublevels by applying the external magnetic field B^{opt} in order to compensate for the imbalance in the transition strengths. This way, a larger atom-probe detuning can be set on the strongest transition.

IV. APPLICATIONS TO ION SYSTEMS

This section gives two numerical applications of the theoretical model developed in the previous section with actual experimental parameters: the first with a symmetric Λ -system and the second with an asymmetric Λ -system. In both cases, the quantization axis is chosen along the axis of the cavity to get rid of the π transitions (i.e. with no change in magnetic quantum number). If needed, the external magnetic field will be applied along this axis. The optical qubit is then encoded in the two orthogonally polarized circular polarizations ($\hat{L} = \hat{a}$ and $\hat{R} = \hat{b}$) associated with the σ^+ and σ^- transitions. We consider Fabry-Perot resonators that can be conventional macroscopic cavities or fiber-based Fabry-Perot microcavities [7]. The latter are composed of laser-machined mirrors at the tip of a fiber, which allows for higher cou-

pling rates but presents higher intrinsic losses. Note that we considered in our model the two polarization modes of the cavity as degenerate in frequency, since situations with no birefringence splitting within the cavity linewidth were observed both in conventional cavities [12] and fiber-based cavities with mirrors designed with a high degree of rotational symmetry [40].

A. Symmetric Λ -system

We first consider the transition ${}^2S_{1/2} - {}^2P_{1/2}$, $F = 1$ to $F' = 0$ in ${}^{171}\text{Yb}^+$ at 329 nm, with a spontaneous emission rate into free space $\gamma = 2\pi \times 9.8$ MHz. As pictured in Fig. 3, $|\downarrow\rangle = \{m_F = -1\}$ - $|e\rangle = \{m_{F'} = 0\}$ and $|\uparrow\rangle = \{m_F = 1\}$ - $|e\rangle = \{m_{F'} = 0\}$ are the two transitions of the Λ -system, with strengths of equal magnitude $C_\downarrow = -C_\uparrow = 1/\sqrt{3} := C$.

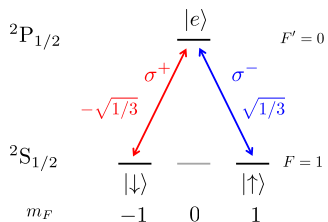


Figure 3. Level configuration of the transition between the ${}^2S_{1/2}$ ($F=1$) and the ${}^2P_{1/2}$ ($F'=0$) manifolds of ${}^{171}\text{Yb}^+$.

Fig. 4 shows the optimized parameters δ_c^{opt} (a) and δ_a^{opt} (b) as a function of κ_{ex} characterizing the coupling mirror transmission, in the range where the total cooperativity $C_t = \frac{(Cg)^2}{\kappa_t\gamma}$ is bigger than one. The associated optimized fidelity and its associated efficiency are shown in solid blue lines in the frames (c) and (d); they reduce to the black dashed lines if no optimization is performed, i.e. $\delta_c = \delta_a = 0$. In accordance with the comments of Sec. III, the fidelity reaches unity by tuning δ_c and δ_a to δ_c^{opt} and δ_a^{opt} when $\kappa_i \leq \kappa_{ex} \leq \kappa_{ex}^{\text{opt}}$ (white area in Fig. 4). In this range, an analytic derivation shows that the fidelity increases by a quantity that can be approximated by $\frac{A^2}{1+A^2}$ with $A = \left| \frac{\kappa_i}{\kappa_{ex}} - \frac{1}{2C_t} \right|$ compared to the case where no detuning is applied.

Fig. 4 can be directly used for any cavity and ionic transition parameters by replacing the various variables with the analytical expressions reported in Tab. I. As an example, we give the numerical values of these variables in the case of the ionic transition considered here and of a typical macroscopic Fabry-Perot resonator ($\kappa_i = 2\pi \times 10$ kHz and $\kappa_i \leq \kappa_{ex} \leq 2\pi \times 123$ kHz) with a coherent coupling rate $g = 2\pi \times 2$ MHz [8, 12], and in the case of a realistic fiber-based Fabry-Perot resonator ($\kappa_i = 2\pi \times 3$ MHz and $\kappa_i \leq \kappa_{ex} \leq 2\pi \times 50$ MHz) with a coherent coupling rate $g = 2\pi \times 40$ MHz [10, 19, 20].

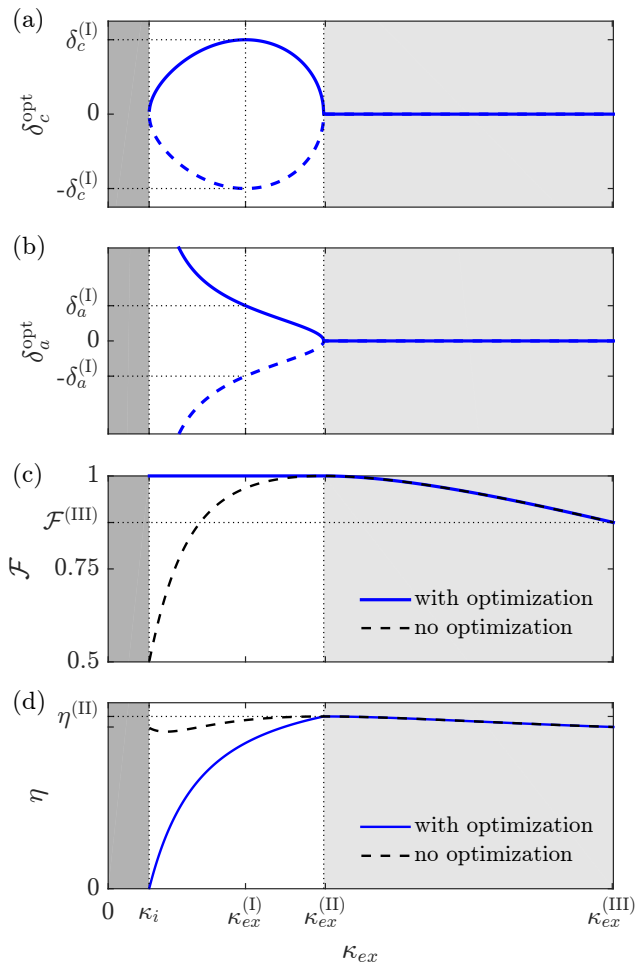


Figure 4. Parameters δ_c^{opt} (a) and δ_a^{opt} (b) leading to unit swap fidelity within the interval $[\kappa_i, \kappa_{ex}^{(II)} = \kappa_{ex}^{\text{opt}}]$ as a function of κ_{ex} . (c) and (d) shows the optimized (solid blue line) and non-optimized (black dashed line, i.e. with $\delta_c = \delta_a = 0$) fidelities and associated efficiencies respectively. Analytical expressions and numerical examples of the various parameters are explicated in Tab. I.

The cavity parameters needed to achieve the experimental situations of Tab. I are given in Tab. II: specifically the length L of the Fabry-Perot resonator, its input-output coupling mirror transmission \mathcal{T}_1 , back mirror transmission \mathcal{T}_2 and other intrinsic losses such as mirrors absorption and scattering \mathcal{L} .

Finally, Fig. 5 shows a map of the fidelity as a function of the parameters δ_c and δ_a for a given $\kappa_{ex} = 2\pi \times 20$ kHz: the optimization (point B) leads to a fidelity equal to 1, i.e. an increase of 17% compared to the situation where no detuning is applied (point A).

	Analytical expression	typical conventional Fabry-Perot	realistic fiber-based Fabry-Perot
κ_i		$2\pi \times 10$ kHz	$2\pi \times 3$ MHz
$g_{\downarrow,\uparrow} = \mathcal{C}g$		$2\pi \times 1.2$ MHz	$2\pi \times 23$ MHz
γ		$2\pi \times 10$ MHz	$2\pi \times 10$ MHz
$\kappa_{ex}^{(I)}$	$\frac{\kappa_i}{2} \sqrt{\frac{4 + 8C_i + 3C_i^2}{1 + C_i}}$	$2\pi \times 34$ kHz	$2\pi \times 11$ MHz
$\kappa_{ex}^{(II)} = \kappa_{ex}^{opt}$	$\kappa_i \sqrt{1 + 2C_i}$	$2\pi \times 52$ kHz	$2\pi \times 18$ MHz
$\kappa_{ex}^{(III)} = \kappa_{ex}(C_t = 1)$	$\kappa_i(C_i - 1)$	$2\pi \times 123$ kHz	$2\pi \times 50$ MHz
$\delta_c^{(I)}$	$\frac{\kappa_i C_i}{2\sqrt{1 + C_i}}$	$2\pi \times 18$ kHz	$2\pi \times 6.2$ MHz
$\delta_a^{(I)}$	$\gamma \sqrt{1 + C_i}$	$2\pi \times 38$ MHz	$2\pi \times 43$ MHz
$\mathcal{F}^{(III)}$	$\frac{4(C_i - 1)^2}{20 - 16C_i + 5C_i^2}$	0.87	0.86
$\eta^{(II)} = \eta_{max}$	$\left(\frac{C_i}{\sqrt{1 + 2C_i} + (1 + C_i)} \right)^2$	0.46	0.51
$\eta^{(III)}$	$\frac{20 - 16C_i + 5C_i^2}{9C_i^2}$	0.43	0.46

Table I. Analytical expressions of the parameters of Fig. 4, and numerical values for the cases of a conventional and a fiber-based Fabry-Perot resonator.

	Analytical expression	typical conventional Fabry-Perot	realistic fiber-based Fabry-Perot
L		20 mm	400 μ m
\mathcal{T}_1		85 ppm	600 ppm
\mathcal{T}_2		1 ppm	30 ppm
\mathcal{L}		15 ppm	70 ppm
Finesse F	$\frac{2\pi}{\mathcal{T}_1 + \mathcal{T}_2 + \mathcal{L}}$	6.2×10^4	9.0×10^3
κ_t	$\frac{\pi c}{2L\mathcal{F}}$	$2\pi \times 60$ kHz	$2\pi \times 21$ MHz
κ_{ex}	$\frac{c\mathcal{T}_1}{4L}$	$2\pi \times 50$ kHz	$2\pi \times 18$ MHz
κ_i	$\frac{c(\mathcal{T}_2 + \mathcal{L})}{4L}$	$2\pi \times 10$ kHz	$2\pi \times 3$ MHz

Table II. Possible cavity parameters for the two above configurations of Tab. I, with c the light velocity.

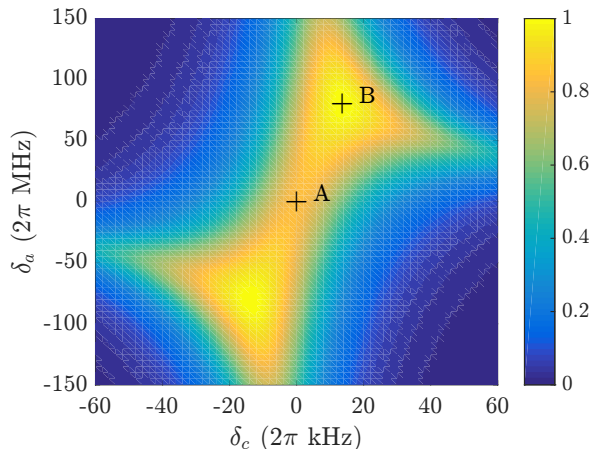


Figure 5. Map of the fidelity as a function of the parameters δ_c and δ_a for $\kappa_{ex} = 2\pi \times 20$ kHz: the point A indicates $\delta_c = \delta_a = 0$ and leads to $\mathcal{F} \simeq 0.83$, and the point B indicates δ_c^{opt} and δ_a^{opt} and leads to $\mathcal{F} = 1$.

B. Asymmetric Λ -system

Next, we consider the transition ${}^2D_{3/2} - {}^2P_{1/2}$ of a ${}^{40}\text{Ca}^+$ ion at 866 nm or ${}^{138}\text{Ba}^+$ at 650 nm, where $(\gamma_{\text{Ca}}, \gamma_{\text{Ba}}) = 2\pi \times (11.2, 9.8)$ MHz $\simeq 2\pi \times 10$ MHz. As pictured in Fig. 6(a), a Λ -system can be isolated from the level structure by considering for instance the two transitions $|\downarrow = \{m_J = -3/2\}\rangle - |e = \{m_J = -1/2\}\rangle$ and $|\uparrow = \{m_J = 1/2\}\rangle - |e = \{m_J = -1/2\}\rangle$ via an initial classical preparation, with no possible leakage to the other Zeeman sublevels. Note however that the ${}^2D_{3/2}$ manifold being metastable ($\tau_{\text{Ca}} = 1$ sec, $\tau_{\text{Ba}} = 18$ sec), the ion can decay to the ${}^2S_{1/2}$ manifold. Nonetheless, discarding this event by postselection will not affect the fidelity of SPRINT. Here the Clebsch-Gordan coefficients are $(\mathcal{C}_\downarrow, \mathcal{C}_\uparrow) = (\sqrt{1/2}, \sqrt{1/6})$: in this asymmetric configuration, the optimization of the fidelity can benefit from the use of an external magnetic field. The Zeeman shifts associated with these transitions are shown in Fig. 6(b).

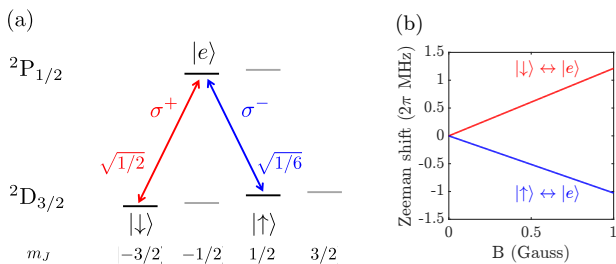


Figure 6. Transition ${}^2D_{3/2} - {}^2P_{1/2}$ of ${}^{40}\text{Ca}^+$: (a) level configuration and (b) Zeeman splitting as a function of the magnetic field B .

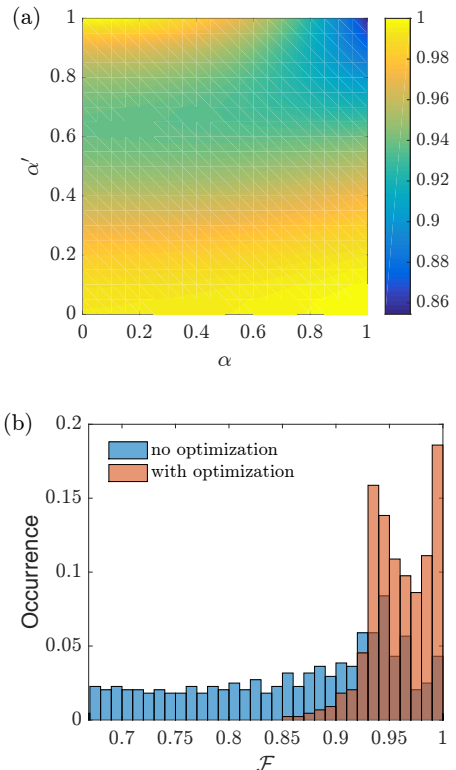


Figure 7. (a) Map of the fidelity as a function of the qubit parameters α and α' for $(\kappa_i, \kappa_{ex}) = 2\pi \times (10, 40)$ kHz and $(g, \gamma) = 2\pi \times (2, 10)$ MHz, with numerically optimized parameters $\delta_c^{\text{opt}} = 2\pi \times 21$ kHz, $\delta_a^{\text{opt}} = 2\pi \times 34$ MHz and $B^{\text{opt}} = 11$ G. (b) Fidelity histograms without (blue) and with (red) optimization of the parameters.

Following Sec. III, a numerical optimization of the parameters δ_c , δ_a and B is performed in order to maximize the fidelity of the SWAP gate for arbitrary input qubits. Fig. 7 pictures this fidelity as a function of the coefficients α and α' characterizing the optical and material qubit respectively in the case of the previously considered macroscopic Fabry-Perot cavity with $(\kappa_i, \kappa_{ex}) = 2\pi \times (10, 40)$ kHz, $g = 2\pi \times 2$ MHz, and for the optimized parameters $\delta_c^{\text{opt}} = 2\pi \times 21$ kHz, $\delta_a^{\text{opt}} = 2\pi \times 34$ MHz and $B^{\text{opt}} = 11$ G. The associated distribution of fidelities is displayed in Fig. 7 (red histogram) and shows an average of $\bar{\mathcal{F}}^{\text{opt}} = 96.0 \pm 2.9\%$, to be compared to $\bar{\mathcal{F}}^0 = 86.5 \pm 9.4\%$ in the case where no optimization is performed (blue histogram).

In Fig. 8, we come back to the two examples of resonator settings considered in Tab. I, that of a macroscopic cavity (frames a to e) and of a fiber-based cavity (frames f to i), and perform the numerical optimization of the fidelity averaged over the input qubits as a function of κ_{ex} . We display the optimal parameters δ_c^{opt} , δ_a^{opt} and B^{opt} (or equivalently the Larmor frequency ω_g^{opt}), the optimized and non-optimized fidelities, and correspond-

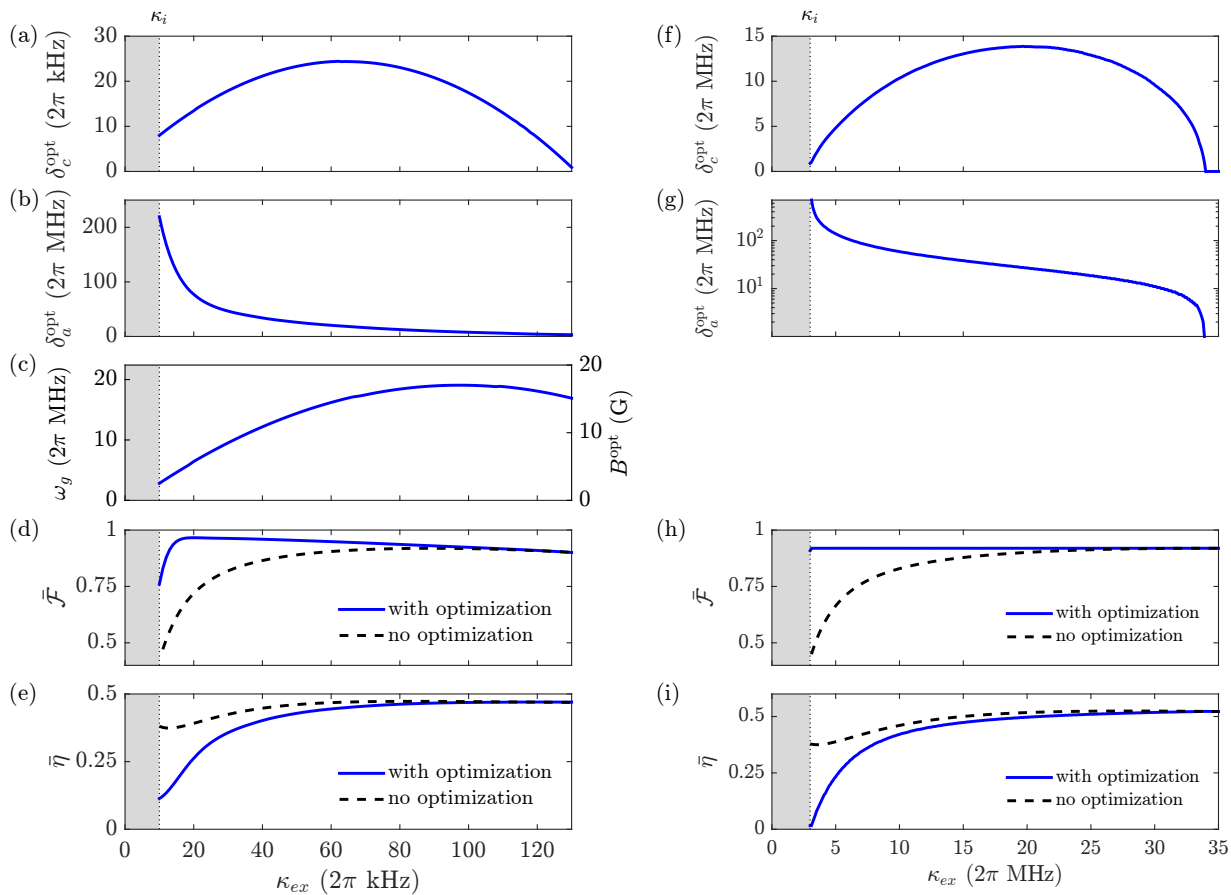


Figure 8. Optimal parameters δ_c^{opt} (frames a and f), δ_a^{opt} (b and g), ω_g^{opt} and corresponding B^{opt} (c) as a function of κ_{ex} . The resulting average fidelities $\bar{\mathcal{F}}$ (d and h) and efficiencies $\bar{\eta}$ (e and i) are shown as solid blue lines, while the non-optimized fidelities and efficiencies are shown as dashed black lines. On the left (frames a to e), typical conventional Fabry-Perot parameters: $\kappa_i = 2\pi \times 10$ kHz and $g = 2\pi \times 2$ MHz; on the right (frames f to i), $B = 0$ G and realistic fiber-based Fabry Perot parameters: $\kappa_i = 2\pi \times 3$ MHz and $g = 2\pi \times 40$ MHz.

ing efficiencies. In the conventional Fabry-Perot configuration, the maximal increase in the average fidelity is found at $\kappa_{ex} = 2\pi \times 20$ kHz and amounts to 25 % (from $\bar{\mathcal{F}}^0 = 72\%$ to $\bar{\mathcal{F}}^{\text{opt}} = 97\%$), while the associated efficiency decreases by 13 % (from $\bar{\eta}^0 = 39\%$ to $\bar{\eta}^{\text{opt}} = 26\%$). In the fiber-based Fabry-Perot configuration, the optimal applied magnetic fields would be too high to be experimentally reasonable (typically up to several kG): this originates from the higher intrinsic losses of such cavities. We then chose to perform the optimization with no applied magnetic field, which still leads in this case to a fair improvement of the fidelity to a mostly identical value of $\bar{\mathcal{F}}^{\text{opt}} = 92\%$. For instance, choosing $\kappa_{ex} = 2\pi \times 8$ MHz leads to an increase in fidelity of 13 % and a decrease in efficiency of 5 %.

V. SUMMARY

This paper demonstrated the feasibility of implementing an ion-photon qubit SWAP gate in realistic trapped ion systems, based on the deterministic single-photon Raman interaction. Importantly, this scheme requires Purcell enhancement but not necessarily strong coupling: in other words, small mode area but a reasonably long cavity that can prevent ions to be too close from the dielectric surfaces for better trap stability.

This theoretical analysis gave the framework to the swap protocol, in particular by discussing the relevant parameters leading to optimize its performance. Specifically, in the case of an equally weighted three-level Λ -system, we showed that there exists a range of extrinsic coupling rates where an appropriate tuning of the probe-cavity and probe-atom frequency detunings restores the fidelity to unity, however at the price of a decrease in

the efficiency. In addition to these detunings, the degeneracy of the Zeeman sublevels can be lifted to further optimize the fidelity in the case of an unequally weighted three-level Λ -system. We quantitatively applied our model to realistic systems, involving state-of-the-art conventional and fiber-based Fabry-Perot cavities, and $^{171}\text{Yb}^+$, $^{40}\text{Ca}^+$ and $^{138}\text{Ba}^+$ ions.

This scheme, highly scalable and ns-fast, is therefore a powerful building block that can be further exploited to realize photon-photon quantum gates, in particular

universal ones such as $\sqrt{\text{SWAP}}$ [28] or C-phase [41].

ACKNOWLEDGEMENTS

Support from the Israeli Science Foundation, the Minerva Foundation and the Crown Photonics Center is acknowledged. This research was made possible in part by the historic generosity of the Harold Perlman family.

-
- [1] H. J. Kimble, *Nature* **453**, 1023 (2008).
 - [2] L. Luo, D. Hayes, T. Manning, D. Matsukevich, P. Maunz, S. Olmschenk, J. Sterk, and C. Monroe, *Fortschritte der Physik* **57**, 1133 (2009).
 - [3] L.-M. Duan and C. Monroe, *Rev. Mod. Phys.* **82**, 1209 (2010).
 - [4] C. Monroe and J. Kim, *Science* **339**, 1164 (2013).
 - [5] T. Northup and R. Blatt, *Nat. Photon.* **8**, 356 (2014).
 - [6] P. F. Herskind, A. Dantan, J. P. Marler, M. Albert, and M. Drewsen, *Nat. Phys.* **5**, 494 (2009).
 - [7] D. Hunger, T. Steinmetz, Y. Colombe, C. Deutsch, T. W. Hänsch, and J. Reichel, *New J. Phys.* **12**, 065038 (2010).
 - [8] A. Stute, B. Casabone, B. Brandstätter, D. Habicher, H. Barros, P. Schmidt, T. Northup, and R. Blatt, *Appl. Phys. B* **107**, 1145 (2012).
 - [9] J. Sterk, L. Luo, T. Manning, P. Maunz, and C. Monroe, *Phys. Rev. A* **85**, 062308 (2012).
 - [10] B. Brandstätter, A. McClung, K. Schüppert, B. Casabone, K. Friebe, A. Stute, P. O. Schmidt, C. Deutsch, J. Reichel, R. Blatt, *et al.*, *Rev. Sci. Instr.* **84**, 123104 (2013).
 - [11] M. Steiner, H. M. Meyer, C. Deutsch, J. Reichel, and M. Köhl, *Phys. Rev. Lett.* **110**, 043003 (2013).
 - [12] A. Stute, B. Casabone, B. Brandstätter, K. Friebe, T. Northup, and R. Blatt, *Nat. Photon.* **7**, 219 (2013).
 - [13] H. Takahashi, A. Wilson, A. Riley-Watson, F. Oručević, N. Seymour-Smith, M. Keller, and W. Lange, *New J. Phys.* **15**, 053011 (2013).
 - [14] M. Cetina, A. Bylinskii, L. Karpa, D. Gangloff, K. M. Beck, Y. Ge, M. Scholz, A. T. Grier, I. Chuang, and V. Vuletić, *New J. Phys.* **15**, 053001 (2013).
 - [15] M. Steiner, H. Meyer, J. Reichel, and M. Köhl, *Phys. Rev. Lett.* **113**, 263003 (2014).
 - [16] B. Casabone, K. Friebe, B. Brandstätter, K. Schüppert, R. Blatt, and T. Northup, *Phys. Rev. Lett.* **114**, 023602 (2015).
 - [17] A. M. Eltony, D. Gangloff, M. Shi, A. Bylinskii, V. Vuletić, and I. L. Chuang, *Quantum Information Processing* **15**, 5351 (2016).
 - [18] A. Márquez Seco, H. Takahashi, and M. Keller, *Atoms* **4**, 15 (2016).
 - [19] T. Ballance, H. Meyer, P. Kobel, K. Ott, J. Reichel, and M. Köhl, *Phys. Rev. A* **95**, 033812 (2017).
 - [20] H. Takahashi, E. Kassa, C. Christoforou, and M. Keller, arXiv preprint arXiv:1808.04031 (2018).
 - [21] H. J. Kimble, *Physica Scripta* **1998**, 127 (1998).
 - [22] M. Harlander, M. Brownnutt, W. Hänsel, and R. Blatt, *New J. Phys.* **12**, 093035 (2010).
 - [23] S. X. Wang, G. Hao Low, N. S. Lachenmyer, Y. Ge, P. F. Herskind, and I. L. Chuang, *J. Appl. Phys.* **110**, 104901 (2011).
 - [24] L.-M. Duan and H. Kimble, *Phys. Rev. Lett.* **92**, 127902 (2004).
 - [25] B. Hacker, S. Welte, G. Rempe, and S. Ritter, *Nature* **536**, 193 (2016).
 - [26] D. Pinotsi and A. Imamoglu, *Phys. Rev. Lett.* **100**, 093603 (2008).
 - [27] G. Lin, X. Zou, X. Lin, and G. Guo, *Europhys. Lett.* **86**, 30006 (2009).
 - [28] K. Koshino, S. Ishizaka, and Y. Nakamura, *Phys. Rev. A* **82**, 010301 (2010).
 - [29] J. Gea-Banacloche and L. M. Pedrotti, *Phys. Rev. A* **83**, 042333 (2011).
 - [30] S. Rosenblum, S. Parkins, and B. Dayan, *Phys. Rev. A* **84**, 033854 (2011).
 - [31] J. Gea-Banacloche and L. M. Pedrotti, *Phys. Rev. A* **86**, 052311 (2012).
 - [32] S. Rosenblum, A. Borne, and B. Dayan, *Phys. Rev. A* **95**, 033814 (2017).
 - [33] O. Bechler, A. Borne, S. Rosenblum, G. Guendelman, O. E. Mor, M. Netser, T. Ohana, Z. Aqua, N. Drucker, R. Finkelstein, Y. Lovsky, R. Bruch, D. Gurovich, E. Shafir, and D. Dayan, *Nat. Phys.* **1000**, 996 (2018).
 - [34] E. Purcell, *Phys. Rev.* **69**, 681 (1946).
 - [35] I. Shomroni, S. Rosenblum, Y. Lovsky, O. Bechler, G. Guendelman, and B. Dayan, *Science* **345**, 903 (2014).
 - [36] S. Rosenblum, O. Bechler, I. Shomroni, Y. Lovsky, G. Guendelman, and B. Dayan, *Nat. Photon.* **10**, 19 (2016).
 - [37] H. Carmichael, *Phys. Rev. Lett.* **70**, 2273 (1993).
 - [38] G. K. Gulati, H. Takahashi, N. Podoliak, P. Horak, and M. Keller, *Sci. Rep.* **7**, 5556 (2017).
 - [39] C. Gardiner and M. Collett, *Phys. Rev. A* **31**, 3761 (1985).
 - [40] H. Takahashi, J. Morphew, F. Oručević, A. Noguchi, E. Kassa, and M. Keller, *Opt. Expr.* **22**, 31317 (2014).
 - [41] Y. Tokunaga and K. Koshino, in *European Quantum Electronics Conference* (Optical Society of America, 2015) p. EB.P-7.